ChemComm

COMMUNICATION

View Article Online
View Journal | View Issue

Cite this: *Chem. Commun.*, 2018, **54**, 13395

Received 10th October 2018,
Accepted 7th November 2018

DOI: 10.1039/c8cc08096h

rsc.li/chemcomm

J-Aggregate squaraine nanoparticles with bright NIR-II fluorescence for imaging guided photothermal therapy†

Pengfei Sun, ‡[a] Qi Wu,‡[a] Xiaoli Sun,[a] Han Miao,[b] Weixing Deng,[a] Wansu Zhang,[a] Quli Fan *[a] and Wei Huang[c]

We introduce a novel strategy to enhance the fluorescence brightness of organic-molecule-based nanoparticles in the second near-infrared window (NIR-II, 1000–1700 nm) by fabricating J-aggregate nanoparticles SQP-NPs$_{(J)}$. Our prepared J-aggregate nanoparticles SQP-NPs$_{(J)}$ show an emission maximum near 1100 nm, and the emission intensity is 4.8-fold higher than that of H-aggregate SQP-NPs$_{(H)}$. In addition, SQP-NPs$_{(J)}$ can be used for NIR-II imaging guided photothermal therapy on MCF-7 tumor-bearing mice due to the fact that SQP-NPs$_{(J)}$ have highly effective photothermal properties, which are significant for precise tumor diagnostics and treatments.

Optical imaging can afford high sensitivity and spatial resolution for early diagnosis of tumors and imaging-guided therapy.[1,2] Nevertheless, optical imaging is limited because photon scattering by biological tissues at the conventional NIR-I (700–900 nm) ranges leads to small imaging penetration depths.[3,4] In the second near-infrared (NIR-II) window ranges from 1000 to 1700 nm, light scattering and photon absorption by biological moieties are minimal, which allow for deeper penetration, micro-scale resolution and an improved signal to background ratio in fluorescence imaging.[5,6] Thus, NIR-II fluorescence imaging shows great promise in meeting the present unsatisfied optical imaging requirements.[7]

Currently, many inorganic NIR-II imaging contrast agents have been developed including single-walled carbon nanotubes (SWNTs),[8] transition-metal sulfide/oxide semiconductors[9] and lanthanide-based downconversion nanoparticles (DCNPs).[10] However, the long-term toxicological profile of inorganic nanomaterials still requires further assessment.[11] In contrast, organic probes, including conjugated polymers and small molecules, enjoy considerable advantages due to their relatively good biocompatibility and easy chemical design, which provide high fluorescence quantum yields.[12] However, most of the organic molecules are inherently hydrophobic, leading to unavoidable molecular aggregation and severe fluorescence quenching when loaded into hydrophilic polymer matrices or modified with ionic groups to realize water-solubility.[13] To overcome this limitation, recently, Liu's group introduced the aggregation-induced emission (AIE) strategy to solve the fluorescence quenching problem in the NIR-II region.[14] However, in the AIE strategy, the AIE electron donor group must be strictly selected, which limited its wide range of applications. Therefore, there are still needs for the development of new strategies to solve the molecular aggregation and fluorescence quenching problems.

Among many kinds of molecule aggregations, J-aggregation is a type of ordered aggregation that results in a ''slipped stack'' arrangement (head–tail).[15] Such J-aggregation molecular assembly of dyes results in strong red-shifted absorption and enhanced fluorescence intensities.[16] To date, a few studies have reported that J-aggregates can be applied in visible and NIR-I region fluorescence imaging. Research by Würthner and co-workers revealed that the J-aggregates of perylene bisimide derivatives exhibit far-red fluorescence and high quantum yields.[17] Xu and co-workers also have demonstrated that pyrrolopyrrole cyanine derivative (PCBF) J-aggregates assembled with an amphiphilic block co-polymer (PCL-*b*-POEGMA) can enhance the light-emission intensity of nanoparticles in the NIR-I region.[18] Therefore, controlling the J-aggregates of NIR-II molecules may be a more suitable method to increase the NIR-II fluorescence. However, to the best of our knowledge, no one has ever tried to control the J-aggregates of NIR-II molecules to realize brighter NIR-II fluorescence imaging.

In our work, we exploited one NIR-absorptive dye, SQP (bispyrrole-sq-bispyrrole), as the model molecule to prepare

---

[a] Key Laboratory for Organic Electronics and Information Displays & Jiangsu Key Laboratory for Biosensors, Institute of Advanced Materials (IAM), Jiangsu National Synergetic Innovation Center for Advanced Materials (SICAM), Nanjing University of Posts & Telecommunications, 9 Wenyuan Road, Nanjing 210023, China. E-mail: iamqlfan@njupt.edu.cn

[b] School of Materials Science and Engineering, Georgia Institute of Technology, Atlanta, GA 30332, USA

[c] Shaanxi Institute of Flexible Electronics (SIFE), Northwestern Polytechnical University (NPU), 127 West Youyi Road, Xi'an 710072, Shaanxi, China

† Electronic supplementary information (ESI) available. See DOI: 10.1039/c8cc08096h

‡ These authors contributed equally to this work.

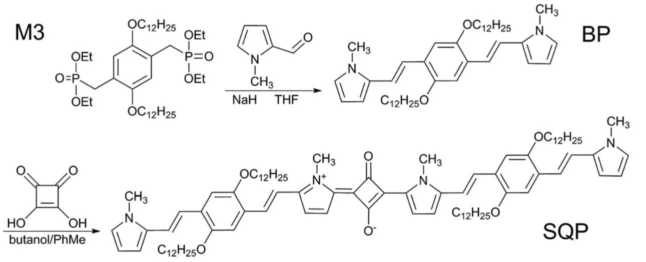

Scheme 1 Synthesis route to SQP.

J-aggregate nanoparticles. Squaraine dyes are widely used fluorescence dyes because they can easily narrow the bandgap to provide strong light-emission in a long wavelength region and have great capability to form J-aggregates in aqueous solution.[19] After encapsulating SQP into an amphiphilic copolymer F-127 (PEG-*b*-PPG-*b*-PEG), J-aggregate SQP-NPs$_{(J)}$ were obtained. Meanwhile, we also prepared H-aggregate (molecules form in a "vertical stack" arrangement, which exhibit a blue-shifted absorption band and weakened fluorescence[20]) SQP-NPs$_{(H)}$ by changing the assembly method. As expected, the NIR-II emission intensity of the SQP-NPs$_{(J)}$ was 4.8-fold higher than that of the SQP-NPs$_{(H)}$ at the same concentration. After applying the two NPs in *in vitro* and *in vivo* NIR-II fluorescence imaging, the brighter signal on MCF-7 cells and the sharper image quality of healthy mice proved the superiority of the SQP-NPs$_{(J)}$. In addition, the NIR-absorbing SQP-NPs$_{(J)}$ can convert laser energy into thermal energy, which endows the SQP-NPs$_{(J)}$ with efficient photothermal therapy (PTT) performance. Therefore, the SQP-NPs$_{(J)}$ were applied in NIR-II imaging guided photothermal therapy (Scheme 1).

SQP was prepared based on previous literature reports, with (*E*,*E*)-1,4-bis[2-(1-methylpyrrol-2-yl)vinyl]-2,5-didodecyloxybenzene (BP) and squaric acid used as the electron donor and acceptor, respectively.[21] Meanwhile, each benzene ring was modified with two alkyl (dodecyl) side chains for enhancing the solubility of the SQP in organic solvents. Condensation of squaric acid with two equivalents of BP at 112 °C afforded the target SQP in 13% yield. The chemical structure of the SQP was characterized using ^{1}H NMR, matrix-assisted laser desorption/ionization time-of-flight mass spectrometry and FT-IR spectroscopy (Fig. S4, S6 and S7, ESI†). The photophysical properties of SQP are presented in Fig. 1a, where the normalized UV-vis-NIR absorption spectra of SQP show a sharp absorption band at 766 nm in THF with a high mass extinction coefficient of 126.3 L g^{-1} cm^{-1} (Fig. S9, ESI†). The fluorescence emission spectra of SQP display main emission peaks at 794 nm and two shoulder peaks at 855 and 1000 nm.

With the SQP dye in hand, an amphiphilic copolymer (PEG-*b*-PPG-*b*-PEG, F-127) was introduced to prepare water-soluble SQP nanoparticles by a co-precipitation method. In the self-assembly process, the SQP dye was dissolved in DCM or THF to prepare J-aggregate nanoparticles (SQP-NPs$_{(J)}$) and H-aggregate nanoparticles (SQP-NPs$_{(H)}$). As we can see from dynamic light scattering (DLS) analysis (Fig. 1b), the hydrodynamic radii (R_h) were 53 ± 2 and 52 ± 2 nm, and the polydispersity indices (PDI) were 0.27 and 0.26 for the SQP-NPs$_{(J)}$ and SQP-NPs$_{(H)}$, respectively.

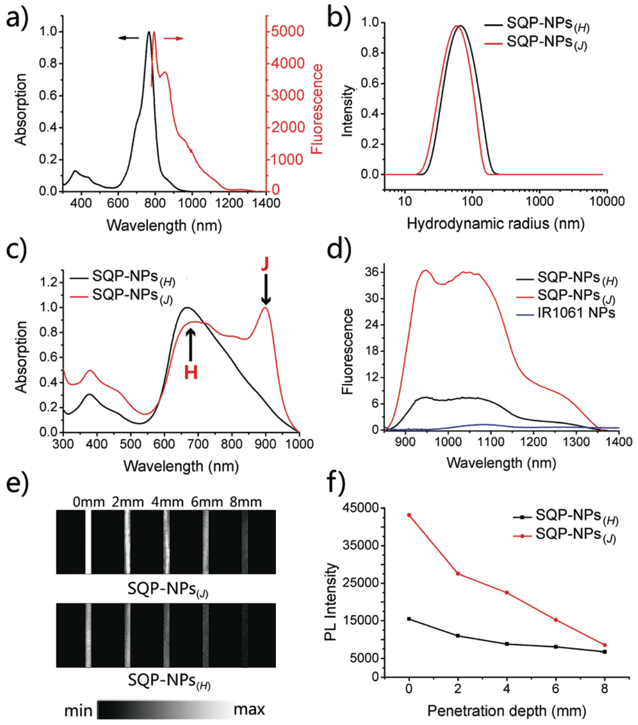

Fig. 1 (a) The absorption spectra and fluorescence emission spectra of SQP in THF. The fluorescent emission spectra were obtained under 730 nm excitation; (b) DLS data of the SQP-NPs$_{(J)}$ and SQP-NPs$_{(H)}$ in water. (c) UV-vis-NIR absorption spectra of the SQP-NPs$_{(J)}$ and SQP-NPs$_{(H)}$; (d) NIR-II fluorescence emission spectra of the SQP-NPs$_{(J)}$, SQP-NPs$_{(H)}$ and IR1061 NPs at the same concentration of 10 μg mL^{-1} under 808 nm excitation; (e) NIR-II fluorescence images of the SQP-NPs$_{(J)}$ and SQP-NPs$_{(H)}$ at different depths; (f) NIR-II fluorescence intensity of the SQP-NPs$_{(J)}$ and SQP-NPs$_{(H)}$ at different depths.

The TEM images (Fig. S10, ESI†) show that both SQP-NPs$_{(J)}$ and SQP-NPs$_{(H)}$ have stable spherical shapes in water with sizes of approximately 82 and 86 nm. These results revealed that the solvent selection of SQP does not have an apparent effect on the size of the nanoparticles.

It is well known that a red-shift or blue-shift in the absorption spectra can be used to characterize the J-aggregates or H-aggregates of dyes.[22] As shown in Fig. 1c, the UV-vis-NIR absorption spectra of the SQP-NPs$_{(J)}$ show one blue-shifted absorption band at 695 nm and another sharp, red-shifted absorption band at 901 nm. Similar to many other research studies,[23,24] this sharp, red-shifted absorption band at 901 nm suggests that SQP has formed J-aggregates in the SQP-NP$_{(J)}$ aqueous solution. In contrast, the SQP-NPs$_{(H)}$ only exhibit a blue-shifted absorption band at 670 nm, which hints the major H-aggregates of SQP in the SQP-NPs$_{(H)}$ aqueous solution.

To verify the ability of J-aggregate nanoparticles in enhancing the fluorescence intensity, the fluorescence emission spectrum of the SQP-NPs$_{(J)}$ was investigated and compared with that of the SQP-NPs$_{(H)}$. As presented in Fig. 1d, the SQP-NPs$_{(J)}$ and SQP-NPs$_{(H)}$ have the same broad emission band extending to 1400 nm, with two peaks at 947 nm and 1036 nm. However, the emission intensity of the SQP-NPs$_{(J)}$ was 4.8-fold higher than that of the SQP-NPs$_{(H)}$ at the same concentration, proving the superiority of the J-aggregate SQP-NPs$_{(J)}$. Apparently, it was the

J-aggregates abundantly formed in the SQP-NPs$_{(J)}$ that contributed to the enhanced NIR-II emission. In addition, the emission intensity of the SQP-NPs$_{(J)}$ was stronger about 35-fold compared to that of the reported NIR-II probe IR1061 NPs, suggesting the exceptionally brighter NIR-II fluorescence of the SQP-NPs$_{(J)}$.

For further detecting the maximum imaging depth of the SQP-NPs$_{(J)}$ and comparing the brightness with the SQP-NPs$_{(H)}$, two tubes filled with the two nanoparticles were placed under pork with different thicknesses, and the NIR-II images were acquired, respectively (Fig. 1e and f). The images of the SQP-NPs$_{(J)}$ were clearly much brighter than those of the SQP-NPs$_{(H)}$, reflecting the benefit of the J-aggregates. Fig. 1f shows the emission intensity of the two SQP-NPs at different depths. It is obvious that the SQP-NPs$_{(J)}$ show a much larger fluorescence intensity compared to that of the SQP-NPs$_{(H)}$ at 2–6 mm of depth. Overall, these results suggest that the NIR-II imaging depth of the two SQP-NPs all reached up to approximately 8 mm.

To study the fluorescence enhancement effect of the SQP-NPs$_{(J)}$ *in vitro*, the NIR-II fluorescence images of MCF-7 cells incubated with the two NPs were measured. As shown in Fig. 2a, the NIR-II image of the MCF-7 cells incubated with the SQP-NPs$_{(J)}$ was obviously brighter than that of the SQP-NPs$_{(H)}$. Accordingly, the fluorescence intensity of the MCF-7 cells incubated with the SQP-NPs$_{(J)}$ was 4.1-fold higher than that of the SQP-NPs$_{(H)}$, reflecting that the SQP-NPs$_{(J)}$ can realize brighter NIR-II imaging at the cellular level.

Next, *in vivo* NIR-II fluorescence imaging measurements were conducted on healthy BALB/c mice for further comparing the imaging capacity of the two nanoparticles. From Fig. 2b, we can distinctly see that the brightness of the cerebral vessels of the mice injected with the SQP-NPs$_{(J)}$ was much higher than that of the SQP-NPs$_{(H)}$. Then, we captured a part of the images indicated by the circled regions (labelled 1–2) on the mice brain, and the NIR-II fluorescence intensity (Fig. 2c) of region 1 was 4.7-fold higher than that of region 2, illustrating the superior brightness of the SQP-NPs$_{(J)}$ *in vivo*. Furthermore, the magnified images of the partial vessel regions (labelled 3–4) on the mice body also demonstrated that the vasculature of the mice injected with the SQP-NPs$_{(J)}$ was much clearer than that of the SQP-NPs$_{(H)}$, suggesting that the SQP-NPs$_{(J)}$ can indeed reach significantly sharper image quality *in vivo*.

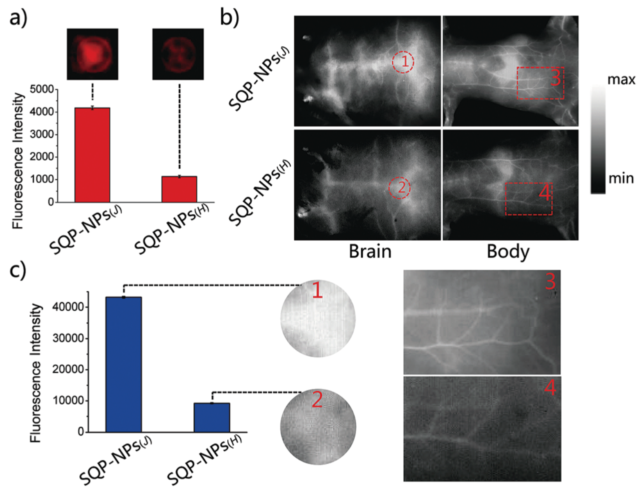

Fig. 2 (a) NIR-II fluorescence intensity of the MCF-7 cells incubated with SQP-NPs$_{(J)}$ and SQP-NPs$_{(H)}$. Inset: NIR-II fluorescence images of the MCF-7 cells incubated with SQP-NPs$_{(J)}$ and SQP-NPs$_{(H)}$; (b) NIR-II fluorescence images of mice brain and mice body after intravenous administration with 2 mg mL^{-1} SQP-NPs$_{(J)}$ and SQP-NPs$_{(H)}$; (c) magnified images of the circled regions (labelled 1–2) and vessel regions (labelled 3–4), as well as the average fluorescence intensity of regions 1–2.

Normally, NIR-absorbing materials can convert laser energy into heat.[25,26] Therefore, the photothermal behaviour of the SQP-NPs$_{(J)}$ was studied. The temperature of the SQP-NPs$_{(J)}$ at a concentration of 100 μg mL^{-1} was increased from 24 °C to 67 °C, while the temperature of deionized water was only increased by 3 °C under the same conditions (Fig. S13a, ESI†). Furthermore, the photothermal conversion efficiency of the SQP-NPs$_{(J)}$ was 36% (Fig. S13d, ESI†), which is high enough for effective photothermal therapy.

To analyse the *in vitro* PTT efficacy of the SQP-NPs$_{(J)}$, an MTT assay, confocal laser scanning microscopy (CLSM) and flow cytometry analysis were used to monitor the cytotoxicity to MCF-7 cells. As shown in Fig. S14a (ESI†), the MCF-7 cells only incubated with 100 μg mL^{-1} SQP-NPs$_{(J)}$ exhibited 92% cell viability, but showed only 27% cell viability after LED lamp irradiation. In the CLSM images (Fig. S14b, ESI†), the MCF-7 cells only treated with the SQP-NPs$_{(J)}$ or LED lamp irradiation showed green fluorescence. In contrast, the MCF-7 cells treated with the SQP-NPs$_{(J)}$ and LED lamp irradiation showed red fluorescence, which reflected obvious cell death. As shown in the flow cytometry image (Fig. S14c, ESI†), the amount of late apoptotic cells increased from 0.56% to 96.8% after LED lamp irradiation when incubated with the SQP-NPs$_{(J)}$. These results testify that SQP-NPs$_{(J)}$ hold great promise to act as PTT agents for tumor treatment.

To further explore the potential application of SQP-NPs$_{(J)}$ in NIR-II imaging-guided therapy, a MCF-7 tumor bearing mouse was treated with SQP-NPs$_{(J)}$ and observed under a NIR-II fluorescence imaging system. The magnified images of the tumor regions are presented in Fig. 3a. Shortly after the intravenous administration of the SQP-NPs$_{(J)}$, the blood vessels of the tumor could be clearly identified with respect to the surrounding background tissue. However, as the time increased, the NIR-II fluorescence signal of the vasculature gradually weakened, but a bright signal inside the tumor enhanced. 24 h after injection, the quantified tumor-to-normal tissue ratio (T/NT) (Fig. 3b) reached the maximum value (3.54 ± 0.2) and the vessel signal completely vanished. These subtle signal changes were not possible to be observed in NIR-I window imaging (Fig. S22, ESI†), which illustrates that NIR-II imaging can provide more precise information about biological diagnoses.

After precise NIR-II fluorescence imaging and diagnosis, SQP-NPs$_{(J)}$ were further used to conduct *in vivo* photothermal therapy on MCF-7 tumor-bearing nude mice. These mice were randomly divided into four groups (six mice per group): (i) saline, (ii) saline with LED lamp treatment, (iii) SQP-NPs$_{(J)}$, and (iv) SQP-NPs$_{(J)}$ with LED lamp treatment. 24 h after intravenous injection with SQP-NPs$_{(J)}$, the tumor region was

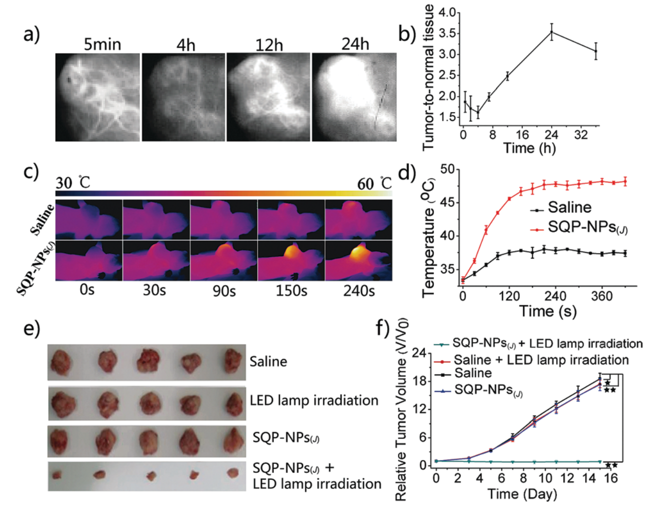

Fig. 3 (a) Magnified NIR-II fluorescence images of tumor regions at different post injection times after administrating SQP-NPs$_{(J)}$; (b) tumor-to-normal tissue (T/TN) ratio of the tumor sites at different times after intravenous injection with SQP-NPs$_{(J)}$; (c) IR thermal images of tumor-bearing mice after intravenous injection with saline and SQP-NPs$_{(J)}$ under LED light lamp (810 nm 0.8 W cm^{-2}) at indicated time point; (d) quantitative analysis of the temperature of the tumor areas of mice as a function of irradiation time; (e) photos of different groups of tumors of mice after therapy for 14 days; (f) tumor growth curves of different groups of MCF-7 tumor-bearing mice after treatment. Ordinates are normalized to their initial size.

exposed to LED irradiation for 10 min. Fig. 3c and d show that the tumor surface temperature of the mice injected with the SQP-NPs$_{(J)}$ reached a maximum of 48 °C but that of the saline group only increased 3 °C, proving the efficient PTT effect of the SQP-NPs$_{(J)}$ *in vivo*. In order to evaluate the inhibitory effects of the SQP-NPs$_{(J)}$ *in vivo*, a time-consuming PTT test were performed. We monitored the tumor volume, tumor weight and body weight every 2 days after treatment. The results showed that the tumors of group iv were nearly eliminated after 15 days (Fig. 3e, f and Fig. S27, ESI†), with a relative low tumor volume and mild tumor weight. Furthermore, no significant body weight loss was observed in all the mice groups (Fig. S28, ESI†), confirming only a slight side effect exist in the PTT treatment. The *in vivo* toxicity of the SQP-NPs$_{(J)}$ was also studied as it is critical for fluorescent labels. The blood chemical and biochemical indicators and pathological images displayed almost no changes (Fig. S29 and S30, ESI†), suggesting the high biosafety of the SQP-NPs$_{(J)}$.

In conclusion, we have successfully prepared a new type of NIR-II probe based on the J-aggregates of squaraine dyes, realizing NIR-II fluorescence imaging-guided PTT. And our study provides unprecedented routes for the preparation of a variety of J-aggregate molecule NIR-II probes for use in high-resolution *in vivo* fluorescence imaging.

This work was financially supported by the National Natural Science Foundation of China (No. 21604042, 21674048 and 21574064), the Synergetic Innovation Center for Organic Electronics and Information Displays, the 333 project of Jiangsu province (No. BRA2016379), and the Primary Research & Development Plan of Jiangsu Province (BE2016770).

Conflicts of interest

There are no conflicts to declare.

Notes and references

1 R. Wissleder and V. Ntziachristos, *Nat. Med.*, 2003, **9**, 123.
2 V. Shanmugam, S. Selvakumar and C. S. Yeh, *Chem. Soc. Rev.*, 2014, **43**, 6254–6287.
3 J. C. Li, J. H. Rao and K. Y. Pu, *Biomaterials*, 2018, **155**, 217–235.
4 Y. Y. Jiang, P. K. Upputuri, C. Xie, L. L. Zhang, Q. H. Xiong, M. Pramanik and K. Y. Pu, *Nano Lett.*, 2017, **17**, 4964–4969.
5 Y. F. Tang, Y. Y. Li, X. M. Hu, H. Zhao, Y. Ji, L. Chen, W. B. Hu, W. S. Zhang, X. Li, X. M. Lu, W. Huang and Q. L. Fan, *Adv. Mater.*, 2018, 1801140.
6 J. J. Zhou, J. Yuan, S. Hou, P. K. Upputuri, D. Wu, J. C. Li, P. Wang, X. Zhen, M. Pramanik, K. Y. Pu and H. W. Duan, *ACS Nano*, 2018, **12**, 2643–2651.
7 J. Qi, C. W. Sun, A. Zebihula, H. Q. Zahng, R. T. K. Kwok, X. Y. Zhao, W. Xi, J. W. Y. Lam, J. Qian and B. Z. Tang, *Adv. Mater.*, 2017, **29**, 1603443.
8 K. Welsher, S. P. Sherlock and H. J. Dai, *Proc. Natl. Acad. Sci. U. S. A.*, 2011, **208**, 8943–8948.
9 C. N. Zhu, P. Jiang, Z. L. Zhang, D. L. Zhu, Z. Q. Tian and D. W. Pang, *ACS Appl. Mater. Interfaces*, 2013, **5**, 1186–1189.
10 Y. L. Yang, P. Y. Wang, L. F. Lu, Y. Fan, C. X. Sun, L. L. Fan, C. J. Xu, A. M. El-Toni, M. Alhoshan and F. Zhang, *Anal. Chem.*, 2018, **90**, 7946–7952.
11 C. Yin, X. Zhen, Q. L. Fan, W. Huang and K. Y. Pu, *ACS Nano*, 2017, **11**, 4172–4182.
12 C. Cui, Z. Yang, X. Hu, J. J. Wu, K. Q. Shou, H. H. Ma, C. Jian, Y. Zhao, B. W. Qi, X. M. Hu, A. X. Yu and Q. L. Fan, *ACS Nano*, 2017, **11**, 3298–3310.
13 S. P. F. Kenry, Y. K. Duan and B. Liu, *Adv. Mater.*, 2018, 1802394.
14 Z. H. Sheng, B. Guo, D. H. Hu, S. D. Xu, W. B. Wu, W. H. Liew, K. Yao, J. Y. Jiang, C. B. Liu, H. R. Zheng and B. Liu, *Adv. Mater.*, 2018, 1800766.
15 S. Senqupta, F. Würthner and F. Chlorophyll, *Acc. Chem. Res.*, 2013, **46**, 2498–2512.
16 S. Kim, T. K. An, J. Chen, S. H. Kang, D. S. Chuang, C. E. Park, Y. Kim and S. Kwon, *Adv. Funct. Mater.*, 2011, **21**, 1616–1623.
17 T. E. Kaiser, H. Wang, V. Stepanenko and F. Würthner, *Angew. Chem., Int. Ed.*, 2007, **46**, 5541–5544.
18 C. J. Yang., X. C. Wang, M. F. Wang, K. M. Xu and C. J. Xu, *Chem. – Eur. J.*, 2017, **23**, 4310–4319.
19 F. Würthner, T. E. Kaiser and C. R. Saha-Möller, *Angew. Chem., Int. Ed. Engl.*, 2011, **50**, 3376–3410.
20 H. J. Chen, M. S. Farahat, K. Y. Law and D. G. Whitten, *J. Am. Chem. Soc.*, 1996, **11**, 2584–2594.
21 D. E. Lynch, U. Geissler and K. A. Byriel, *Synth. Met.*, 2001, **124**, 385–391.
22 Z. Q. Yan, H. Y. Xu, S. Y. Guang, X. Zhao, W. L. Fan and X. Y. Liu, *Adv. Funct. Mater.*, 2012, **22**, 345–352.
23 H. Berlepch and C. Böttcher, *Langmuir*, 2013, **29**, 4948–4958.
24 K. Ouchi, C. L. Colyer, M. Sebaiy., J. Zhou, T. Maeda, H. Nakazumi, M. Shibukawa and S. Saito, *Anal. Chem.*, 2015, **87**, 1933–1940.
25 Y. Lyu, Y. Fang, Q. Q. Miao, X. Zhen, D. Dan and K. Y. Pu, *ACS Nano*, 2016, **10**, 4472–4481.
26 W. X. Deng, Q. Wu, P. F. Sun, P. C. Yuan, X. M. Lu, Q. L. Fan and W. Huang, *Polym. Chem.*, 2018, **9**, 2805–2812.